

Correct criterion of crustal failure driven by intense magnetic stress in neutron stars

YASUFUMI KOJIMA¹

¹ *Department of Physics, Graduate School of Advanced Science and Engineering,
Hiroshima University, Higashi-Hiroshima, Hiroshima 739-8526, Japan*

(Dated: August 27, 2024)

ABSTRACT

Magnetar outbursts are powered by an intense magnetic field. The phenomenon has recently drawn significant attention because of a connection to some fast radio bursts that has been reported. Understanding magnetar outbursts may provide the key to mysterious transient events. The elastic deformation of the solid crust due to magnetic field evolution accumulates over a secular timescale. Eventually, the crust fractures or responds plastically beyond a particular threshold. Determination of the critical limit is required to obtain the shear strain tensor in response to magnetic stress. In some studies, the tensor was substituted with an approximate expression determined algebraically from the magnetic stress. This study evaluated the validity of the approximation by comparing it with the strain tensor obtained through appropriate calculations. The differential equations for the elastic deformation driven by the magnetic field were solved. The results indicated that the approximation did not represent the correct strain tensor value, both in magnitude and spatial profile. Previous evolutionary calculations based on spurious criteria are likely to overestimate the magnitude of the strain tensor, and crustal failure occurs on a shorter timescale. Therefore, revisiting evolutionary calculations using the correct approach is necessary. This study is essential for developing the dynamics of crustal fractures and the magnetic-field evolution in a magnetar.

Keywords: Neutron stars; Compact objects; Magnetars; High-energy astrophysics

1. INTRODUCTION

Magnetars are a peculiar class of neutron stars characterized by their variability which is driven by intense magnetic fields (Duncan & Thompson 1992). The X-ray luminosity is very bright in the range 10^{32} – 10^{36} erg/s, which exceeds the spin-down luminosities of most sources. Frequent bursting activity is also observed in soft gamma repeaters (SGRs). Short bursts typically last for 0.1–1 s, and the peak luminosity is 10^{39} – 10^{41} erg/s. More energetic outbursts also occur, including extreme events such as a giant flare, in which energy over 10^{44} erg is released in a moment (Turolla et al. 2015; Kaspi & Beloborodov 2017; Esposito et al. 2021, for a review). Bursting events with larger energies are inevitably rare. The energy supply for persistent emissions and transient bursts and flares observed in magnetars can be explained by the magnetic energy $\sim 10^{45}(B/10^{14}\text{G})^2$ erg stored in the interior star or exterior magnetosphere with a typical field strength B . Magnetars probably possess more magnetic energy in their reserve because the interior toroidal magnetic field is 10^2 times stronger than that of the surface dipole, as observationally suggested from the spin precession (Makishima et al. 2014, 2016, 2021a,b).

Strong magnetic fields cause significant stress in the crust, and the strain increases over time. When the crust can no longer support the stress, it fractures, leading to soft gamma and X-ray emissions in the magnetosphere (Thompson & Duncan 1995). The crust-fracturing model resembles an earthquake, although with a different triggering force. Magnetic reconnection in the magnetosphere has been proposed as another outburst model in close analogy with solar flares (Lyutikov 2003). The external magnetic fields become twisted over long periods owing to the plastic motion of the crust. When the magnetosphere loses equilibrium beyond a certain threshold, a catastrophic transition results in an outburst or flare.

SGR bursts, earthquakes, solar flares, and other transient events may share some common statistical properties. One notable relationship is the power-law dependence of the number of bursts on their energy (Cheng et al. 1996; Göğüş et al. 1999; Göğüş et al. 2000, for SGR bursts), known as the Gutenberg–Richter law for earthquakes.

Such statistical arguments regarding SGRs have attracted considerable attention recently because of a class of fast radio bursts (FRBs) which has been associated with a magnetar, SGR J1935+2154 (Bochenek et al. 2020; CHIME/FRB Collaboration et al. 2020). However, such a repeating source might not be representative, and FRBs are, therefore, still mysterious events (e.g., Zhang 2020; Petroff et al. 2022, for reviews). The similar statistical properties between SGRs and repeating FRBs have been extensively studied to explore their connection. The scale-invariant energy feature was analyzed using the Tsallis q-Gaussian distribution (Wei et al. 2021; Sang & Lin 2022). The correlation function between a pair of FRBs over a short timescale was explored, revealing a close similarity with that of earthquakes and the short bursts from the magnetar, SGR J1935+2154, but different from solar flares (Totani & Tsuzuki 2023; Tsuzuki et al. 2024). However, for longer intervals beyond the one-second threshold, a unified scaling law in the temporal occurrence revealed a functional similarity in functional form to solar flares rather than earthquakes (Du et al. 2024). Arrival time patterns of magnetar bursts and repeating FRBs were compared within the framework of chaos and randomness (Zhang et al. 2024; Yamasaki et al. 2024). In the energy domain, SGR bursts are consistent with earthquakes, solar flares, and FRBs, whereas SGR bursts are less random than other transient phenomena. Despite significant efforts, sufficient understanding of the similarity or dissimilarity between magnetar bursts and other transient phenomena is lacking.

The power-law form frequently emerges in various phenomena and is characterized by a self-organized criticality (SOC) feature (Bak et al. 1987), that models complexities in nature without a detailed microscopic structure. This concept has been applied to various phenomena, including earthquakes (Bak et al. 2002), solar flares (Aschwanden 2015; Aschwanden et al. 2016), gamma-ray bursts (Dănilă et al. 2015), and magnetar bursts (Lander 2023). Detailed simulation on the microscopic scale is impossible, making the SOC concept a useful approach. However, a microscopic understanding of various events is critical to distinguish between them.

How are crust fractures in a magnetar driven by intense magnetic stress (Thompson & Duncan 1995; Levin & Lyutikov 2012; Lander et al. 2015; Thompson et al. 2017)? The failure of solid materials is determined by the strain tensor σ_{ij} . The stable range by widely used criteria is determined by the condition that the difference between the maximum and minimum eigenvalues of σ_{ij} (in the Tresca criterion) or the magnitude $(\sigma_{ij}\sigma^{ij}/2)^{1/2}$ (in the von Mises criterion) is smaller than the critical number. A crust responds elastically when its deformation is within the limit, beyond which it cracks or responds plastically (Jones 2003; Levin & Lyutikov 2012; Beloborodov & Levin 2014). For the strain caused by the magnetic stress, σ is estimated by the shear modulus μ and the change in the magnetic field δB , as $\mu\sigma \sim B\delta B/(4\pi)$ of the order of magnitude (e.g., Thompson & Duncan 1995; Yang & Zhang 2021). In further detailed models, all components of the tensor σ^{ij} are necessary. An approximate relation $\sigma^{ij} = -(2\mu)^{-1}\delta T_{\text{mag}}^{ij}$ was used to determine the elastic limit in the numerical simulations of the Hall magnetic-field evolution (Perna & Pons 2011; Viganò et al. 2013; Dehman et al. 2020), where $\delta T_{\text{mag}}^{ij}$ denotes the change in the magnetic stress tensor. They assumed that the crustal fracture occurred when the approximate strain tensor $\sigma^{ij} = -(2\mu)^{-1}\delta T_{\text{mag}}^{ij}$ satisfied the breakup criterion. They counted such events during their time-evolution simulation, and proposed a model for the observed burst rate based on the data. Another algebraic expression slightly different from $-(2\mu)^{-1}\delta T_{\text{mag}}^{ij}$ was used in the numerical simulation of the critical transition from elastic to plastic states (Lander & Gourgouliatos 2019; Gourgouliatos & Lander 2021), and for modeling crustal fractures (e.g., Lander et al. 2015; Lander 2016; Suvorov & Kokkotas 2019). The explicit expression for the elastic stress tensor algebraically obtained from the magnetic tensor will be discussed in Section 2.

However, the strain tensor cannot be determined using an algebraic equation. Instead, it should be determined by solving the differential equations (e.g., Landau & Lifshitz’s 1970). The elastic deformation of the neutron star has been calculated by solving the differential equations for the nonmagnetized case (e.g., Ushomirsky et al. 2000; Giliberti et al. 2020; Gittins et al. 2021; Kerin & Melatos 2022), and for the magnetized case (Kojima et al. 2021, 2022; Kojima 2022; Kojima et al. 2023; Fujisawa et al. 2023). The calculation is generally time-consuming. When the approximate criterion is good, the previous evolutionary models without the trouble are justified. However, when the criterion is unjustified, evolutionary models should be revisited.

In this study, the validity of the algebraic expression $\sigma^{ij} = -(2\mu)^{-1}\delta T_{\text{mag}}^{ij}$ is considered by solving the differential equations for the elastic deformation driven by the magnetic field. However, the justification for this has not yet been discussed. Therefore, this study is essential for developing the dynamics of crustal fractures and the magnetic-field evolution in a magnetar.

The remainder of this paper is organized as follows. Equations and models used are discussed in Section 2. The shear strain was numerically calculated from magnetic field models. Section 3 compares the numerical results for the elastic stress tensor with those of the magnetic tensor, which was approximately used as an elastic tensor in the literature. Finally, the conclusions are presented in Section 4.

2. MATHEMATICAL FORMULATION

2.1. Crustal model

A crust of neutron stars from the core–crust interface at r_c to the surface at R is considered, and the thickness is assumed to be $\Delta r/R = (R - r_c)/R = 0.1$. The extremely thin outer crust is ignored; therefore, the mass density ranges from $\rho(r_c) = \rho_c = 1.4 \times 10^{14} \text{ g cm}^{-3}$ at the core–crust boundary r_c to the neutron-drip density $\rho(R) = \rho_1 = 4 \times 10^{11} \text{ g cm}^{-3}$. The hydrostatic equilibrium under Newtonian gravity is determined as follows:

$$\frac{dp}{dr} = -\rho g, \quad (1)$$

where $g\vec{e}_r = \vec{\nabla}\Psi_G$ is the gravitational acceleration, which may be approximated as uniform throughout the crust because the crustal mass is extremely smaller than the total mass and the thickness was sufficiently small. The reasonably approximated spatial profiles for the density ρ and pressure p are obtained by

$$\rho = \rho_c[1 - a(r - r_c)]^2, \quad p = p_c[1 - a(r - r_c)]^3, \quad (2)$$

where $a = (1 - (\rho_1/\rho_c)^{1/2})/\Delta r$. The pressure at $r = r_c$, $p_c = 10^{33} \text{ dyn cm}^{-2}$, and decreases $p(R) = p_c(\rho_1/\rho_c)^{3/2} \approx 1.5 \times 10^{-4} p_c \approx 1.5 \times 10^{29} \text{ dyn cm}^{-2}$. The gravitational acceleration is given by $g = 3ap_c/\rho_c \approx 1.7 \times 10^{14} \text{ cm s}^{-2}$.

The shear modulus μ may be approximated as a linear function of ρ , which is overall-fitted to the results of a detailed calculation reported in a previous study (see Figure 43 in [Chamel & Haensel 2008](#)). Thus, μ is given by a radial function, approximated in terms of the crustal spatial density profile

$$\mu = \mu_c[1 - a(r - r_c)]^2, \quad (3)$$

where $\mu_c = 10^{30} \text{ erg cm}^{-3}$ at the core–crust interface.

2.2. Elastic deformation

The following two equilibrium states are considered: One is an initial state balanced without elastic deformation, and the other is balanced with elastic stress because of the magnetic field evolution on a secular timescale. The difference in the force-balance equation corresponding to the two states results in

$$\nabla_j(T_{\text{hyd}}^{ij} + T_{\text{elas}}^{ij} + T_{\text{mag}}^{ij}) - \delta\rho\vec{\nabla}\Phi_G = 0, \quad (4)$$

where T^{ij} is the stress tensor difference for each force ¹, respectively, given by

$$T_{\text{hyd}}^{ij} = -\delta p g^{ij}, \quad (5)$$

$$T_{\text{elas}}^{ij} = 2\mu\sigma^{ij}, \quad (6)$$

$$T_{\text{mag}}^{ij} = \frac{1}{4\pi} \left(B^i B^j - \frac{1}{2} g^{ij} B^2 \right). \quad (7)$$

In Equation (4), the change in the gravitational potential is ignored: $\delta\Phi_G = 0$, that is, the Cowling approximation is used. The deviations are assumed to be so small that linear perturbation was applied. Perturbations in the mass density $\delta\rho$ and the pressure δp are expressed by the Lagrange displacement $\vec{\xi}$;

$$\delta\rho = -\vec{\nabla} \cdot (\rho\vec{\xi}), \quad \delta p = -(\vec{\xi} \cdot \vec{\nabla})p - \Gamma p(\vec{\nabla} \cdot \vec{\xi}), \quad (8)$$

where an adiabatic change in pressure is assumed, and Γ denotes the adiabatic index.

¹ δT^{ij} may be a better expression; however, the notation T^{ij} is used without any confusion because only small first-order changes are considered.

The elastic stress tensor (6) is given by the shear modulus μ and trace-free strain tensor σ_{ij} ;

$$\sigma_{ij} = \frac{1}{2} (\nabla_i \xi_j + \nabla_j \xi_i) - \frac{1}{3} g_{ij} \nabla_k \xi^k, \quad (9)$$

where g_{ij} denotes a three-dimensional metric. Spherical coordinates (r, θ, ϕ) are used, and the explicit components of a vector and tensor are expressed in an orthonormal basis $(\partial_r, r^{-1}\partial_\theta, (r \sin \theta)^{-1}\partial_\phi)$. Axial symmetry, $\partial_\phi = 0$ is assumed for the magnetic field and the displacement to simplify the calculation. The displacement vector $\vec{\xi}$ is expanded in terms of the Legendre polynomials $P_l(\cos \theta)$ and radial functions $R_l(r)$, $U_l(r)$, and $V_l(r)$;

$$[\xi_r, \xi_\theta, \xi_\phi] = \sum_l [rR_l P_l, rU_l P_{l,\theta}, -rV_l P_{l,\theta}], \quad (10)$$

where radial functions U_l and V_l are meaningful for the index $l \geq 1$; however, it is convenient to introduce $U_0 = V_0 = 0$.

Tensor components T_{ij} are generally decomposed in terms of the spherical tensor harmonics and radial functions $a_l(r)$, $b_l(r)$, $c_l(r)$, $d_l(r)$, $f_l(r)$ and $g_l(r)$ as

$$T_{ij} = \sum_l \begin{pmatrix} a_l P_l & b_l P_{l,\theta} & -c_l P_{l,\theta} \\ b_l P_{l,\theta} & f_l W_l + g_l P_l & d_l W_l \\ -c_l P_{l,\theta} & d_l W_l & -f_l W_l + g_l P_l \end{pmatrix}, \quad (11)$$

where $W_l(\theta)$ is an angular function defined as

$$W_l = \sin \theta \left(\frac{P_{l,\theta}}{\sin \theta} \right)_{,\theta}. \quad (12)$$

The lower limit of l in the sum (11) is limited by the fact that $P_{0,\theta} = 0$ and $W_0 = W_1 = 0$. The expression with the index l may be written by using $b_0 = c_0 = d_0 = d_1 = f_0 = f_1 = 0$.

The magnetic field evolution between equilibria is not explicitly considered, because the magnetic field necessary for elastic deformation is obtained only by numerical calculations. Moreover, the change during the evolution depends on the initial conditions. The initial magnetic field used in previous numerical works was chosen arbitrarily because the force-balance including the magnetic force was ignored (Perna & Pons 2011; Viganò et al. 2013; Dehman et al. 2020; Gourgouliatos & Lander 2021). The magnitude of the magnetic field is so small that the effect is neglected in the force-balance equation, whereas the magnetic field is highly constrained by considering equilibrium condition. By avoiding complicated calculations, the magnetic stress tensor T_{mag}^{ij} in Equation (7) is analytically given and the displacement $\vec{\xi}$ is calculated. Unlike the forms of T_{hyd}^{ij} and T_{elas}^{ij} , T_{mag}^{ij} is the quadratic of B^i . This study does not explicitly split B^i into its initial value and an assumed slight variation; instead, a small change in the stress tensor given by the form of T_{mag}^{ij} is assumed. The radial functions in Equation (11) are obtained for the specified magnetic-field model. A potential limitation of using the assumed magnetic field is that the magnetic stress tensor used in this calculation may significantly differ from that of evolved field. This occurrence is expected to be rare, but should be checked in future works.

2.3. Axial perturbation

The axial perturbation ($\xi_r = \xi_\theta = 0, \xi_\phi \neq 0$) is assumed, in which the density and pressure perturbations are decoupled. After separating the angular part, the ϕ component of Equation (4) is reduced to an ordinary differential equation (see e.g., Kojima et al. 2021, 2022)

$$(\mu r^4 V_l' + c_l r^3)' - (l(l+1) - 2)r^2(\mu V_l - d_l) = 0. \quad (13)$$

Here, prime (') denotes a derivative with respect to r . For $l = 1$, Equation (13) is analytically calculated as $\mu r V_1' + c_1 = 0$, where the integration constant is fixed by the boundary condition.

The $r\phi$ and $r\phi$ components are relevant to the axial perturbation, and the elastic stress is explicitly written as

$$T_{\text{elas}}^{r\phi} = 2\mu\sigma^{r\phi} = -\mu \sum_l r V_l' P_{l,\theta}, \quad T_{\text{elas}}^{\theta\phi} = 2\mu\sigma^{\theta\phi} = -\mu \sum_l V_l W_l. \quad (14)$$

The corresponding components of the magnetic stress are given by Equation (11)

$$T_{\text{mag}}^{r\phi} = -\sum_l c_l P_{l,\theta}, \quad T_{\text{mag}}^{\theta\phi} = \sum_l d_l W_l. \quad (15)$$

The condition $T_{\text{elas}}^{i\phi} + T_{\text{mag}}^{i\phi} = 0$ ($i = r, \theta$) leads to $\mu r V_l' + c_l = 0$ and $\mu V_l - d_l = 0$. The function V_l cannot satisfy these equations identically because V_l is determined using Equation (13) for the independent functions c_l and d_l . The relation $T_{\text{elas}}^{i\phi} + T_{\text{mag}}^{i\phi} = 0$ ($i = r, \theta$) cannot be satisfied, and the accuracy of the approximation is examined by solving Equation (13) in Section 3.

2.4. Polar perturbation

For polar perturbations ($(\xi_r, \xi_\theta) \neq 0, \xi_\phi = 0$), tensor components $T^{rr}, T^{\theta\theta}, T^{\phi\phi}$, and $T^{r\theta}$ are relevant, and the density and pressure changes are generally associated with the perturbations. In the Cowling approximation, the perturbation equations were derived (see e.g., McDermott et al. 1988; Ushomirsky et al. 2000). The magnetic stress terms (a_l, b_l, f_l , and g_l) are included in previous studies. However, the variables and notations used herein are slightly different from those reported in previous studies. The r and θ components of Equation (4) are reduced to the following set of fourth-order differential equations:

$$R_l' = \frac{l(l+1)\alpha_2}{\alpha_3 r} U_l - \left(\frac{3\Gamma}{\alpha_3} + \frac{rp'}{\alpha_3 p} \right) \frac{R_l}{r} + \frac{1}{\alpha_3 p r^4} (X_l - a_l r^3), \quad (16)$$

$$U_l' = -\frac{R_l}{r} + \frac{1}{\mu r^4} (Y_l - b_l r^3), \quad (17)$$

$$X_l' = \frac{l(l+1)}{r} Y_l + \left(\frac{3\Gamma}{\alpha_3} + \frac{rp'}{\alpha_3 p} \right) \left(\frac{X_l}{r} - 2l(l+1)\mu r^2 U_l - a_l r^2 \right) - \left[\rho' g r^2 + \frac{(rp')^2}{\alpha_3 p} - 4\mu \left(\frac{3\Gamma}{\alpha_3} + \frac{2rp'}{\alpha_3 p} \right) \right] r^2 R_l + r^2 (a_l + 2g_l), \quad (18)$$

$$Y_l' = -\frac{\alpha_2}{\alpha_3 r} X_l + (l(l+1) - 2) (\mu r^2 U_l + f_l r^2) - \left(\frac{6\Gamma}{\alpha_3} + \frac{2rp'}{\alpha_3 p} \right) \mu r^2 R_l + \frac{3l(l+1)\Gamma}{\alpha_3} \mu r^2 U_l + \frac{r^2}{2} \left[\left(\frac{3\Gamma}{\alpha_3} - 1 \right) a_l - 2g_l \right]. \quad (19)$$

where

$$\alpha_2 = \Gamma - \frac{2\mu}{3p} \approx \Gamma, \quad \alpha_3 = \Gamma + \frac{4\mu}{3p} \approx \Gamma. \quad (20)$$

These functions are approximated as Γ because $\mu \ll p$. The adiabatic constant is assumed to be constant and $\Gamma = 1.5$ is used in the numerical calculations described in Section 3.

The $r\theta$ component of the elastic stress is expressed as

$$T_{\text{elas}}^{r\theta} = 2\mu\sigma^{r\theta} = \sum_l \mu (rU_l' + R_l) P_{l,\theta} = \sum_l \left(\frac{Y_l}{r^3} - b_l \right) P_{l,\theta} = -T_{\text{mag}}^{r\theta} + \sum_l \left(\frac{Y_l}{r^3} \right) P_{l,\theta}, \quad (21)$$

where Equations (11) and (17) are used. The relation $T_{\text{elas}}^{r\theta} + T_{\text{mag}}^{r\theta} = 0$ holds, when $Y_l = 0$. This condition is generally not satisfied.

The relationship between the shear and magnetic tensors in the diagonal part is complicated. The trace of elastic stress tensor T_{elas}^{ij} is zero, whereas that of T_{mag}^{ij} is nonzero. Therefore, the relation $T_{\text{elas}}^{ij} = -T_{\text{mag}}^{ij}$ is assumed only in the off-diagonal region (Perna & Pons 2011; Viganò et al. 2013; Dehman et al. 2020). In order to remove the discrepancy in the trace, the traceless form $\hat{T}_{\text{mag}}^{ij}$ for B^i is proposed to obtain an approximate elastic stress tensor (Lander et al. 2015; Lander 2016; Lander & Gourgouliatos 2019; Suvorov & Kokkotas 2019; Gourgouliatos & Lander 2021); $T_{\text{elas}}^{ij} = -\hat{T}_{\text{mag}}^{ij}$ where

$$\hat{T}_{\text{mag}}^{ij} = \frac{1}{4\pi} \left(B^i B^j - \frac{1}{3} g^{ij} B^2 \right). \quad (22)$$

Moreover, pressure perturbation also affects the relation $T_{\text{elas}}^{ij} = -T_{\text{mag}}^{ij}$ or $T_{\text{elas}}^{ij} = -\hat{T}_{\text{mag}}^{ij}$. Therefore, the relation does not hold in this exact form, and the accuracy of the approximation may be verified by using the numerical calculations

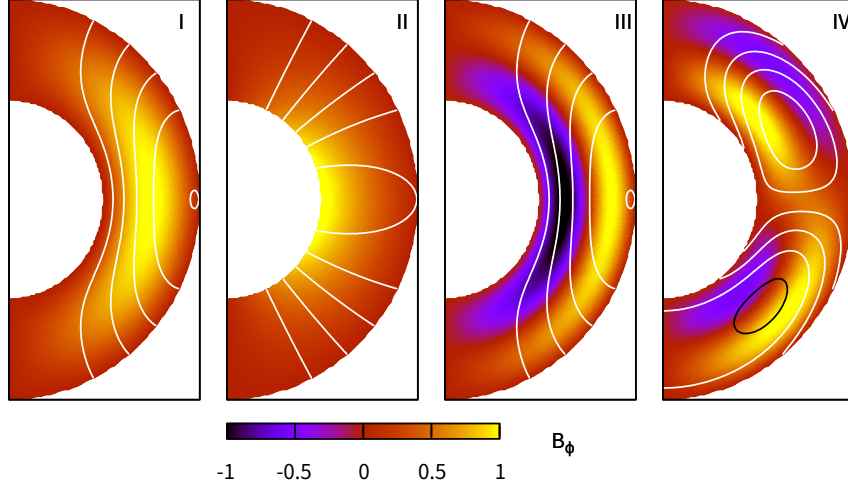


Figure 1. Magnetic field geometry in the crust for four models. Magnetic function $\Psi(r, \theta)$ for a poloidal field is represented by contours, and the field strength of the toroidal component B_ϕ , normalized by the maximum of $|B_\phi|$, is represented by colors. Crustal region is five times enlarged for display.

described in Section 3. However, this comparison may not be appropriate, e.g., for T^{rr} , which depends on the trace of T^{ij} . Therefore, two trace-free combinations, $T^{\theta\theta} - T^{\phi\phi}$ and $2T^{rr} - T^{\theta\theta} - T^{\phi\phi}$ are used to compare the diagonal part. They are unchanged if T_{mag}^{ij} is replaced by $\hat{T}_{\text{mag}}^{ij}$.

2.5. Boundary conditions

The radial component of the total stress tensor $\sum T^{ri}$ ($i = r, \theta, \phi$), i.e., the traction must be continuous across the surfaces at $r = r_c$ and R (see e.g., McDermott et al. 1988; Ushomirsky et al. 2000). For $i = \phi$, the total $T_{\text{elas}}^{r\phi} + T_{\text{mag}}^{r\phi}$ must be continuous. The magnetic component is assumed to be continuous on both sides. This case corresponds to the axial perturbation with ξ_ϕ , and the boundary conditions for the radial function V_l at $r = r_c$ and R can be written as follows:

$$V_l' = 0. \quad (23)$$

Pressure perturbation is involved in polar perturbation. Both T_{hyd}^{ri} and T_{mag}^{ri} are assumed to be continuous to the interior core ($r \leq r_c$) and the exterior ($r \geq R$). The continuity of the rr and $r\theta$ components of the traction at $r = r_c$ and R leads to

$$\begin{aligned} 2rR_l' + l(l+1)U_l = 0, & \iff X_l - (rp' + 3\Gamma p)r^3R_l + \frac{3}{2}l(l+1)\Gamma pr^3U_l = ar^3, \\ rU_l' + R_l = 0, & \iff Y_l = br^3, \end{aligned} \quad (24)$$

where Equations (16) and (17) are used to obtain the second expression.

2.6. Magnetic field in the crust

Model	Magnetic field geometry	Equation	$ B_r/B_0 _{\max}$	$ B_\theta/B_0 _{\max}$	$ B_\phi/B_0 _{\max}$	$(B_{av}/B_0)^2$
I	Dipole expelled from core	(26)	1.02	11.7	1.05	26.5
II	Dipole penetrated to core	(27)	1.37	0.67	1.11	0.93
III	Dipole with strong toroidal field with a node	(28)	1.02	11.7	10.3	63.0
IV	Mixed toroidal-poloidal field with $l = 1$ and 2	(29)	4.18	34.5	2.17	192

Table 1. Description of magnetic model

It is assumed that the external field is a dipole in vacuum ($r \geq R$). The poloidal field is described as $\vec{B}_p = \vec{\nabla} \times (\Psi \vec{e}_\phi / (r \sin \theta))$ in terms of the magnetic function Ψ . The explicit form of Ψ is given by

$$\Psi = -\frac{B_0 R^3}{2r} \sin \theta P_{1,\theta} = \frac{B_0 R^3}{2r} \sin^2 \theta, \quad (25)$$

where B_0 is the field strength at the magnetic pole on the surface $r = R$ and is hereafter used as the normalization constant. The toroidal component B_ϕ disappears on the exterior ($r \geq R$).

The following four models are considered for the crustal magnetic field, which is connected to the dipole in a vacuum at $r = R$. Model I describes the dipolar magnetic field that is expelled from the core. The magnetic function and toroidal component are given by

$$\Psi^I = -\frac{B_0}{2} \left[2R^2 - rR - (R-r)^2 \frac{R(R+\Delta r)}{\Delta r^2} \right] \sin \theta P_{1,\theta}, \quad B_\phi^I = \frac{B_0 R}{r} \sin \left(\frac{\pi(r-R)}{\Delta r} \right) P_{1,\theta}. \quad (26)$$

These functions are displayed in the left panel of Figure 1. Owing to the steep change in Ψ in the radial direction, $|B_\theta|$ increases toward the inner boundary r_c approximately ten times more than the other components, $|B_r|$ and $|B_\phi|$.

In Model II, the poloidal and toroidal components of the magnetic field are smoothly connected from the core to the crust, as displayed in the second panel of Figure 1. The field is described as follows:

$$\Psi^{II} = -\frac{B_0}{2} \left[2R^2 - rR + (R-r)^2 \right] \sin \theta P_{1,\theta}, \quad B_\phi^{II} = \frac{B_0 R}{r} \left(\frac{r-R}{\Delta r} \right) P_{1,\theta}. \quad (27)$$

All components of the magnetic field are comparable in the magnitude $\sim B_0$, although they depend on the spatial position.

In Model III, the poloidal magnetic field is the same as that of Model I, but the toroidal component increases by one order of magnitude. Furthermore, a node exists in the radial direction, that is, B_ϕ changes in the direction, as shown in the third panel of Figure 1. The magnetic field is given by

$$\Psi^{III} = \Psi^I, \quad B_\phi^{III} = 10 \times \frac{B_0 R}{r} \sin \left(\frac{2\pi(r-R)}{\Delta r} \right) P_{1,\theta}. \quad (28)$$

The magnitude of the magnetic field is given by $|B_\theta| \sim |B_\phi| \sim 10 \times |B_r|$.

Finally, Model IV is a combination of $l = 1$ and $l = 2$. A confined component with an angular dependence of $l = 2$ is added to that of Model I, as follows:

$$\Psi^{IV} = \Psi^I + \frac{B_0 R^2}{2} \sin \left(\frac{r-R}{\Delta r} \right) \sin \theta P_{2,\theta}, \quad B_\phi^{IV} = B_\phi^I - \frac{B_0 R}{r} \sin \left(\frac{2\pi(r-R)}{\Delta r} \right) P_{2,\theta}. \quad (29)$$

The toroidal magnetic field with $l = 2$ yields a node in the radial direction.

These functions (Equations (26)–(29)) are examples for convenience to provide the magnetic stress T_{mag}^{ij} which drives the elastic deformation. As discussed in Section 2.2, T_{mag}^{ij} is expressed by B^i , and the models are chosen from various mathematical possibilities with a low multipole index l . The astrophysical situation leading to the magnetic stress T_{mag}^{ij} however is not considered. These models are summarized in Table 1 as shown in Figure 1. The maximum value of each component and the average field strength are also added, calculated in the crust as $B_{\text{av}}^2 \equiv \int B^2 d^3x / \int d^3x$.

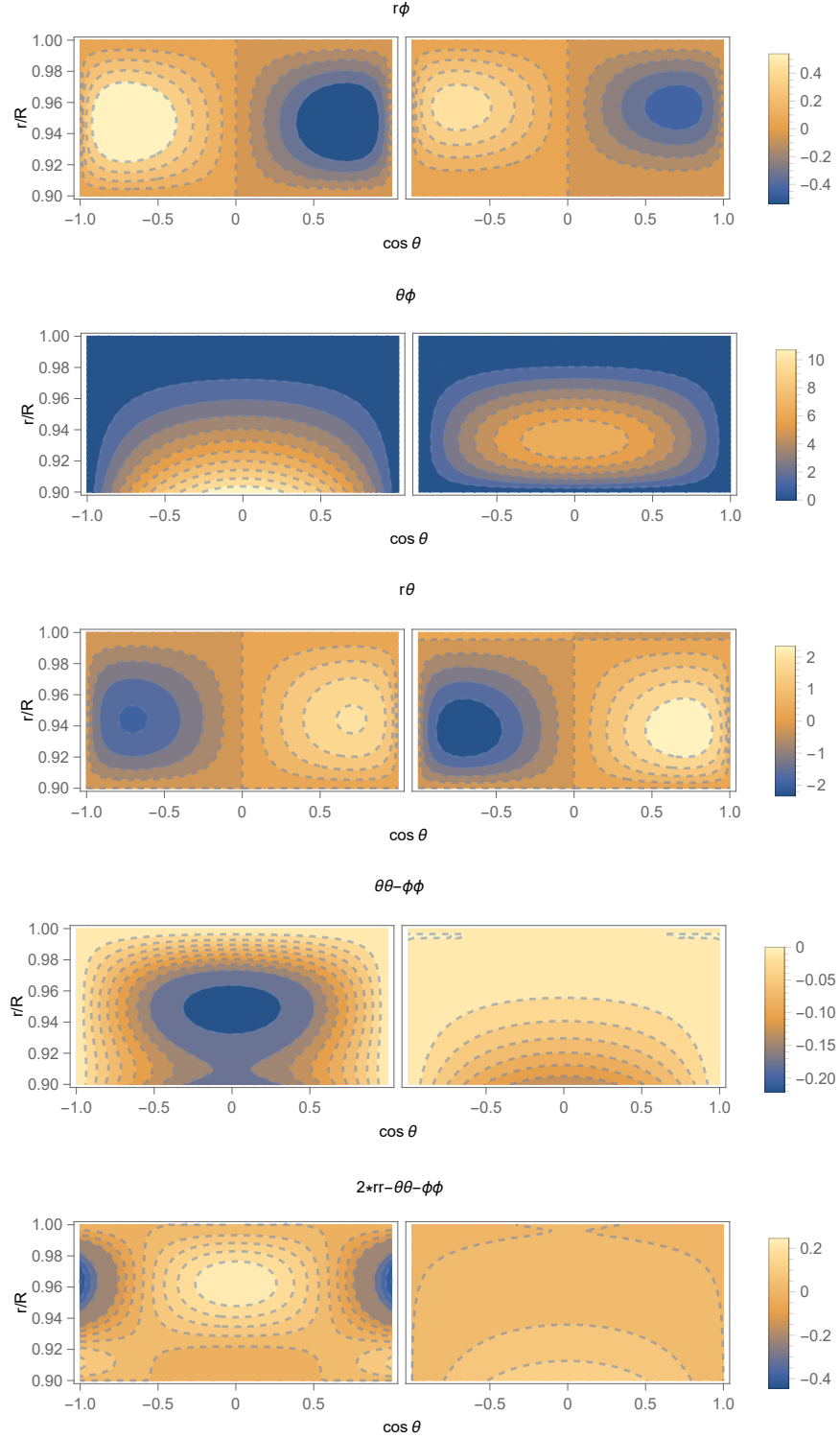


Figure 2. Display of tensor components via contours in the $\cos\theta$ - r/R plane for Model I. The elastic stress T_{elas}^{ij} (left panel) is compared with the magnetic one $-T_{\text{mag}}^{ij}$ (right panel). From the top to bottom columns, $T^{r\phi}$, $T^{\theta\phi}$, $T^{r\theta}$, $T^{\theta\theta} - T^{\phi\phi}$, and $2T^{r\theta} - T^{\theta\theta} - T^{\phi\phi}$ components are shown. In the fourth and fifth panels, the magnetic part is so large that their maximum is adjusted by multiplying by a factor of 10^{-3} .

3. RESULTS

3.1. Comparison between elastic and magnetic tensors

The displacement vector $\vec{\xi}$ is obtained by numerically solving Equations (13) and (16)–(19) for the source terms T_{mag}^{ij} , given by the model described in Section 2.6. The strain tensor (9) is calculated, and the resultant elastic stress $T_{\text{elas}}^{ij} = 2\mu\sigma^{ij}$ is compared with $-T_{\text{mag}}^{ij}$ in Figure 2. The latter is proposed as an approximate form for the elastic stress tensor. The magnitudes of the tensor components are indicated by the contours in the $\cos\theta-r/R$ plane for the magnetic-field Model I. Different components are normalized by a common factor such that the relative comparisons between them are meaningful.

The result suggests that the off-diagonal components of the elastic stress tensor may be approximated as $T_{\text{elas}}^{ij} \sim -T_{\text{mag}}^{ij}$, although their maximum positions differ in the $\theta\phi$ component (second panel of Figure 2). The difference in the radial direction originates from the following boundary values: $T_{\text{mag}}^{\theta\phi} = 0$; however, $T_{\text{elas}}^{\theta\phi} \neq 0$ at $r = r_c$. The boundary conditions for the differential equation (13) are $V_2' = 0$ (Equation (23)), and $T_{\text{elas}}^{\theta\phi} = -V_2W_2$ (Equation (14)) is determined posteriorly and is generally nonzero at $r = r_c$.

As discussed in Section 2.4, T_{elas}^{ij} does not agree with $-T_{\text{mag}}^{ij}$ in the diagonal components; the trace of T_{elas}^{ij} is zero, whereas that of T_{mag}^{ij} is nonzero. Therefore, T_{elas}^{ij} is compared with $-T_{\text{mag}}^{ij}$ using two trace-free combinations of the diagonal components, $T^{\theta\theta} - T^{\phi\phi}$ and $2T^{rr} - T^{\theta\theta} - T^{\phi\phi}$. These results are shown in the fourth and fifth panels of Figure 2. These components differ significantly in magnitude. The magnetic components are approximately three orders of magnitude larger than the elastic components. Therefore, a reduction factor of 10^{-3} is multiplied by in the fourth and fifth panels, respectively. The reason for this large difference is the hydrodynamic terms T_{hyd}^{ij} and $\delta\rho\vec{\nabla}\Phi_G$ in Equation (4). Their ratio to the elastic term is typically $p/\mu \sim 10^3$ by the order-of-magnitude estimate. The elastic stress does not necessarily compensate for the magnetic stress.

The magnitude of the strain tensor σ_{ij} is given by the sum of the axial and polar parts

$$\frac{1}{2}\sigma_{ij}\sigma^{ij} = (\sigma_{\text{ax}})^2 + (\sigma_{\text{po}})^2, \quad (30)$$

with their explicit forms written in terms of the combination of the components as

$$\begin{aligned} (\sigma_{\text{ax}})^2 &= (\sigma^{\theta\phi})^2 + (\sigma^{r\phi})^2 \\ &= \frac{1}{4\mu^2} \left((T_{\text{elas}}^{\theta\phi})^2 + (T_{\text{elas}}^{r\phi})^2 \right), \end{aligned} \quad (31)$$

$$\begin{aligned} (\sigma_{\text{po}})^2 &= \frac{1}{12} (2\sigma^{rr} - \sigma^{\theta\theta} - \sigma^{\phi\phi})^2 + \frac{1}{4} (\sigma^{\theta\theta} - \sigma^{\phi\phi})^2 + (\sigma^{r\theta})^2 \\ &= \frac{1}{48\mu^2} (2T_{\text{elas}}^{rr} - T_{\text{elas}}^{\theta\theta} - T_{\text{elas}}^{\phi\phi})^2 + \frac{1}{16\mu^2} (T_{\text{elas}}^{\theta\theta} - T_{\text{elas}}^{\phi\phi})^2 + \frac{1}{4\mu^2} (T_{\text{elas}}^{r\theta})^2. \end{aligned} \quad (32)$$

In the axial part σ_{ax} , the major component in the magnitude is $|T_{\text{elas}}^{\theta\phi}|$, which differs significantly from $|T_{\text{mag}}^{\theta\phi}|$, although $|T_{\text{elas}}^{r\phi}| \approx |T_{\text{mag}}^{r\phi}|$. In the polar part σ_{po} , the first and second terms in Equation (32) differ from those of the magnetic part. If the diagonal components (T_{elas}^{rr} , $T_{\text{elas}}^{\theta\theta}$, $T_{\text{elas}}^{\phi\phi}$) are replaced by (T_{mag}^{rr} , $T_{\text{mag}}^{\theta\theta}$, $T_{\text{mag}}^{\phi\phi}$) or ($\hat{T}_{\text{mag}}^{rr}$, $\hat{T}_{\text{mag}}^{\theta\theta}$, $\hat{T}_{\text{mag}}^{\phi\phi}$), the magnitude σ_{po} increases significantly, even though $|T_{\text{elas}}^{r\theta}| \approx |T_{\text{mag}}^{r\theta}|$. Thus, the magnitude of the ‘elastic’ tensor approximated by T_{mag}^{ij} is significantly larger than that of the true elastic tensor.

The angular dependence is definite for each tensor component, $(T^{r\theta}, T^{r\phi}) \propto P_{l,\theta}$, $(T^{\theta\phi}, T^{\theta\theta} - T^{\phi\phi}) \propto W_l$, and $2T^{rr} - T^{\theta\theta} - T^{\phi\phi} \propto P_l$. Apart from the trivial angular dependence, radial functions are more suitable for understanding the difference between elastic and magnetic stresses. For the magnetic field Model I, the spherical harmonic index is given by $l = 2$ only, except for $2T^{rr} - T^{\theta\theta} - T^{\phi\phi}$. The latter is a mixture of $l = 0$ and $l = 2$; however, the monopole part of T_{elas}^{ij} is considerably smaller than that of the quadrupole part, as shown by the angular dependence of P_2 provided in the fifth panel of Figure 2. Figure 3 shows their radial functions for $l = 2$. The approximation $T_{\text{elas}}^{ij} \approx -T_{\text{mag}}^{ij}$ is good for the $r\phi$ and $r\theta$ components, as shown in Figure 2. The comparison in the radial profile might be meaningless for the diagonal parts, i.e., $T^{\theta\theta} - T^{\phi\phi}$, and $2T^{rr} - T^{\theta\theta} - T^{\phi\phi}$, because their magnitudes are considerably different for the elastic and magnetic parts.

Figure 4 shows the radial functions for Model II, in which the magnetic field is continuous to the core ($r \leq r_c$) and, therefore, the values at r_c change. Unlike Figure 3, approximation $T_{\text{elas}}^{ij} \approx -T_{\text{mag}}^{ij}$ does not hold for any of the

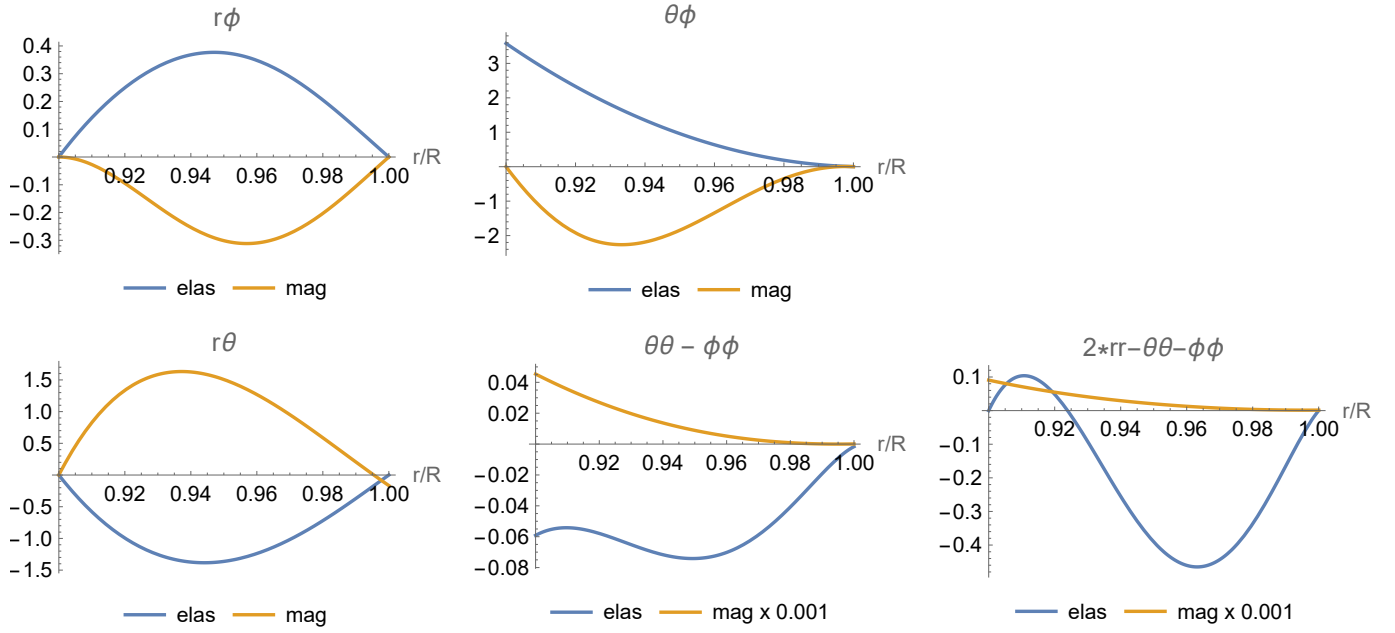


Figure 3. The radial functions for the elastic stress (in blue) and those for the magnetic stress (in orange) are shown for $T^{r\phi}$, $T^{\theta\phi}$, $T^{r\theta}$, $T^{\theta\theta} - T^{\phi\phi}$, and $2T^{rr} - T^{\theta\theta} - T^{\phi\phi}$. A factor of 10^{-3} is multiplied for $T_{\text{mag}}^{\theta\theta} - T_{\text{mag}}^{\phi\phi}$ and $2T_{\text{mag}}^{rr} - T_{\text{mag}}^{\theta\theta} - T_{\text{mag}}^{\phi\phi}$.

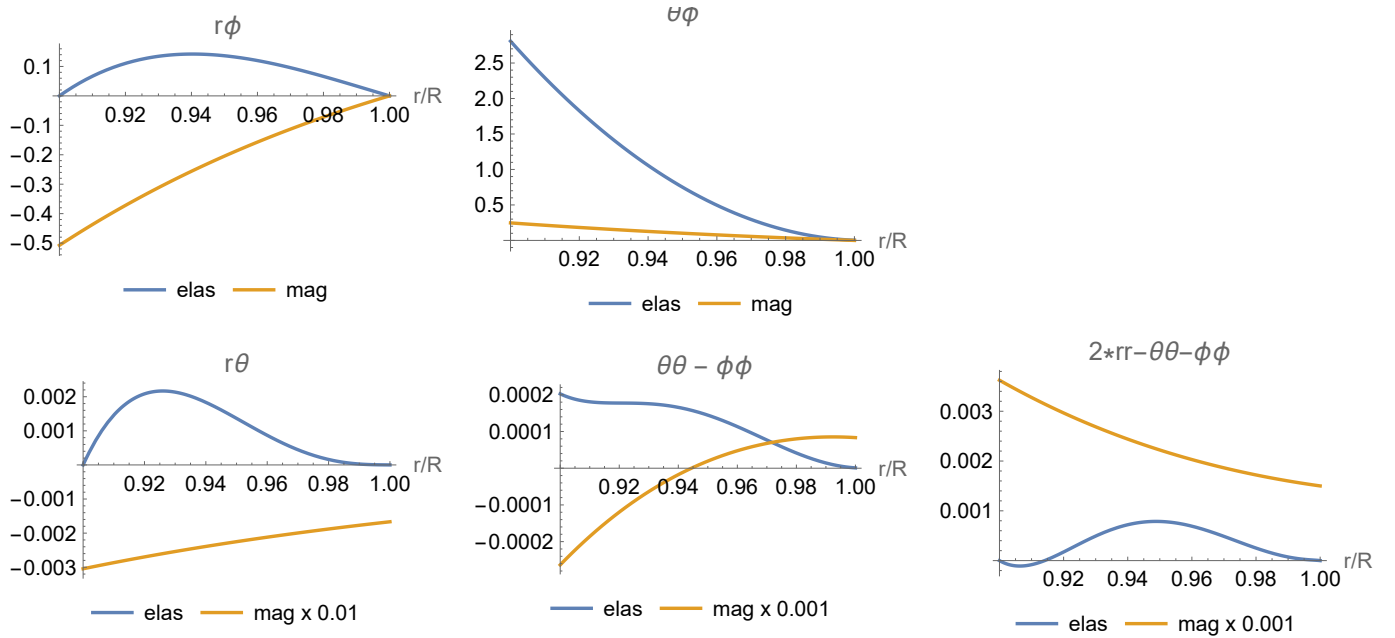


Figure 4. Comparison of the radial function for magnetic model II. The radial function for the magnetic part (in orange) in the bottom row is multiplied by a factor of 10^{-2} , 10^{-3} , and 10^{-3} .

components; it is invalid for the $r\phi$ and $r\theta$ components. This is owing to the boundary value at r_c ; $T_{\text{mag}}^{ri} \neq 0$ ($i = \theta, \phi$) in Model II, whereas $T_{\text{mag}}^{ri} = 0$ in Model I. The elastic stress T_{elas}^{ri} ($i = \theta, \phi$) must disappear, making the accidental coincidence $T_{\text{mag}}^{ri} = 0$ ($i = \theta, \phi$) at r_c necessary for the approximation. $T_{\text{elas}}^{ij} \sim -T_{\text{mag}}^{ij}$ is useless as an estimate in the polar component because the magnitude is significantly different; the elastic stress is two or three orders of magnitude smaller than that of the magnetic stress, as shown by the three panels at the bottom row of Figure 4. The elastic response to the magnetic force is minor in the diagonal component, owing to the presence of hydrodynamic stress

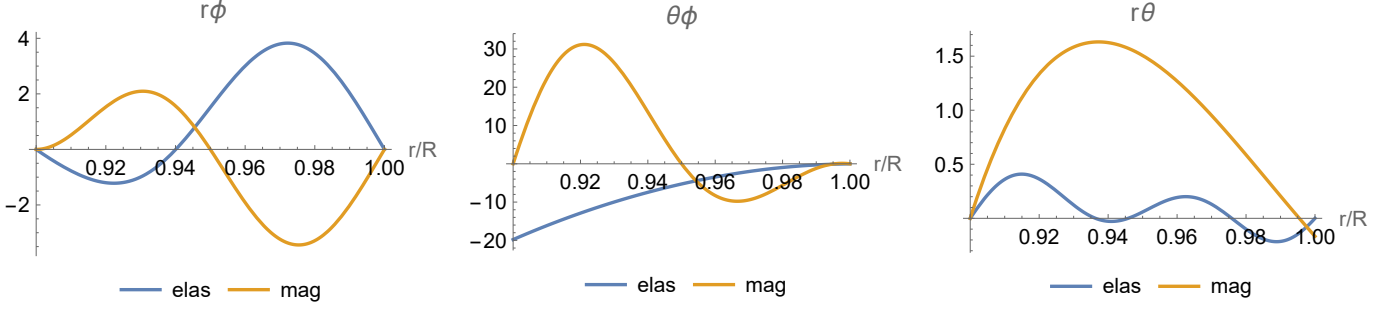


Figure 5. Radial functions for off-diagonal components are compared for Model III. The elastic stress is shown in blue, and the magnetic stress is in orange.

T_{hyd}^{ij} . For the off-diagonal component $T_{\text{elas}}^{r\theta}$, it is coupled with the diagonal component T_{mag}^{ii} through the function Y_l (see Equation (21)). Consequently, a significant imbalance occurs between the elastic and magnetic stresses, and the relationship $T_{\text{elas}}^{ij} \sim -T_{\text{mag}}^{ij}$ is unreliable, even on the order of the estimate.

Next, magnetic Model III is considered, in which the poloidal field is the same as that in Model I. However, the toroidal component is stronger and contains a radial node, as shown in the third panel of Figure 1. The poloidal and toroidal components are comparable in the magnitude. The boundary values of T_{mag}^{ij} both at $r = r_c$ and R are the same as those for Model I. Figure 5 shows the radial functions for the off-diagonal components. In the $r\phi$ component, the approximation $T_{\text{elas}}^{r\phi} \approx -T_{\text{mag}}^{r\phi}$ holds, despite the radial node in $T_{\text{mag}}^{r\phi}$. The approximation worsens in the $r\theta$ -component. The radial function for the magnetic part is the same as that for Model I, as shown in Figure 3 because $T_{\text{mag}}^{r\theta} \propto B^r B^\theta$ is unchanged from that of Model I. However, the resultant $T_{\text{elas}}^{r\theta}$ shown in Figure 5 differs significantly from that in Figure 3; a wavy structure appears in the radial direction because of B_ϕ and the absolute magnitude of the elastic function is reduced. The polar part, $T_{\text{elas}}^{r\theta}$, is significantly affected by the significant strength of B_ϕ^2 .

A more complicated geometry of the magnetic field is considered, as shown in the fourth panel of Figure 1 (Model IV). The poloidal field is a mixture of dipole ($l = 1$) and a confined component of $l = 2$. The toroidal field also comprises confined components with $l = 1$ and 2. The magnetic field is expelled from the core, and the boundary values for B_r and B_ϕ are the same as those for Model I.

The elastic and magnetic stresses in the off-diagonal components were compared. Figure 6 shows T_{elas}^{ij} and $-T_{\text{mag}}^{ij}$ via contour maps in the $\cos\theta$ - r/R plane. The maximum and minimum values of T_{elas}^{ij} approximately trace those of $-T_{\text{mag}}^{ij}$. The radial profiles of the elastic stress are smooth. For example, the two peaks of the magnetic stress in the radial direction are not clearly visible in the elastic stress. Therefore, examining the accuracy of $T_{\text{elas}}^{ij} \approx -T_{\text{mag}}^{ij}$ by eye is no longer useful.

Figure 7 shows radial functions decomposed using angular functions ($T^{r\theta}, T^{r\phi}$) $\propto P_{l,\theta}$ ($l = 1, \dots, 4$), $T^{\theta\phi} \propto W_l$ ($l = 2, \dots, 4$). In the $r\phi$ component (the first row of Figure 7), all functions for the elastic and magnetic stresses vanish at both boundaries. However, the elastic part does not respond locally to the magnetic part in the internal region, except for $l = 1$. Thus, their spatial profile as a sum of these functions becomes significantly different. In the $\theta\phi$ component (the second row of Figure 7), the radial behavior is different in the elastic and magnetic parts; the elastic functions decrease monotonically, whereas the magnetic functions are sinusoidal. This causes a significant difference in the second panel of Figure 6. Finally, in the $r\theta$ component (the third row of Figure 7), the boundary values at $r = R$ differ for $l = 1$ and 3, and the elastic function is less oscillatory. Thus, the approximation $T_{\text{elas}}^{ij} \approx -T_{\text{mag}}^{ij}$ is not justified or requires extremely restrictive conditions.

3.2. Magnitude of the strain tensor

It is useful to show the spatial distribution of the strain tensor magnitude $(\sigma_{ij}\sigma^{ij}/2)^{1/2}$ (Equation (30)), which is relevant to crustal failure according to the von Mises criterion. The quantity indicates which part of the crust is broken under various magnetic fields. Figure 8 shows the normalized quantity σ_* , for which the maximum value is unity. The angular dependence in Model II (top right panel in Figure 8) originates from $W_2(\propto \sin^2\theta)$ because the component $\sigma^{\theta\phi}(\propto W_2)$ is dominant. The slightly complicated angular dependence in Models I and III are superpositions of $\sigma^{\theta\phi} \propto W_2$ and $(\sigma^{r\theta}, \sigma^{r\phi}) \propto \sin\theta \cos\theta$. In Model IV, different l modes are involved, and the spatial profile of σ_* is more

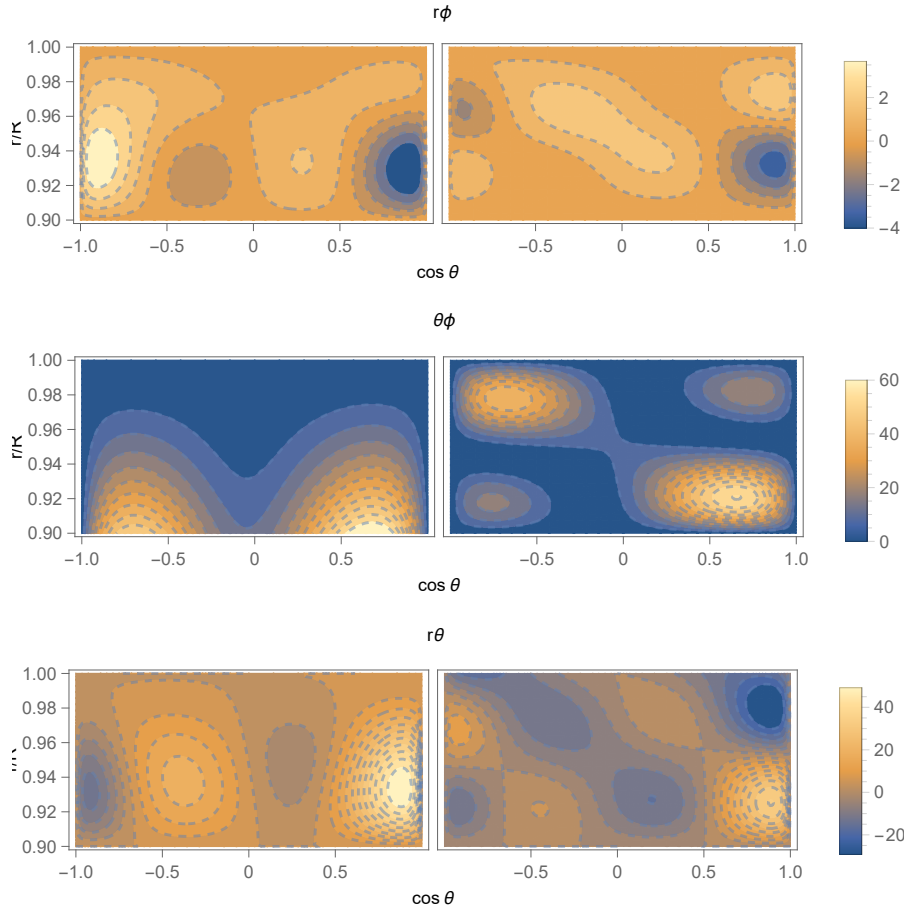


Figure 6. Display of stress components by a contour map in the $\cos\theta$ - r/R plane. The elastic stress T_{elas}^{ij} (left panel) is compared with the magnetic stress $-T_{\text{mag}}^{ij}$ (right panel) for Model IV. From top to bottom, $T^{r\phi}$, $T^{\theta\phi}$, and $T^{r\theta}$ are shown.

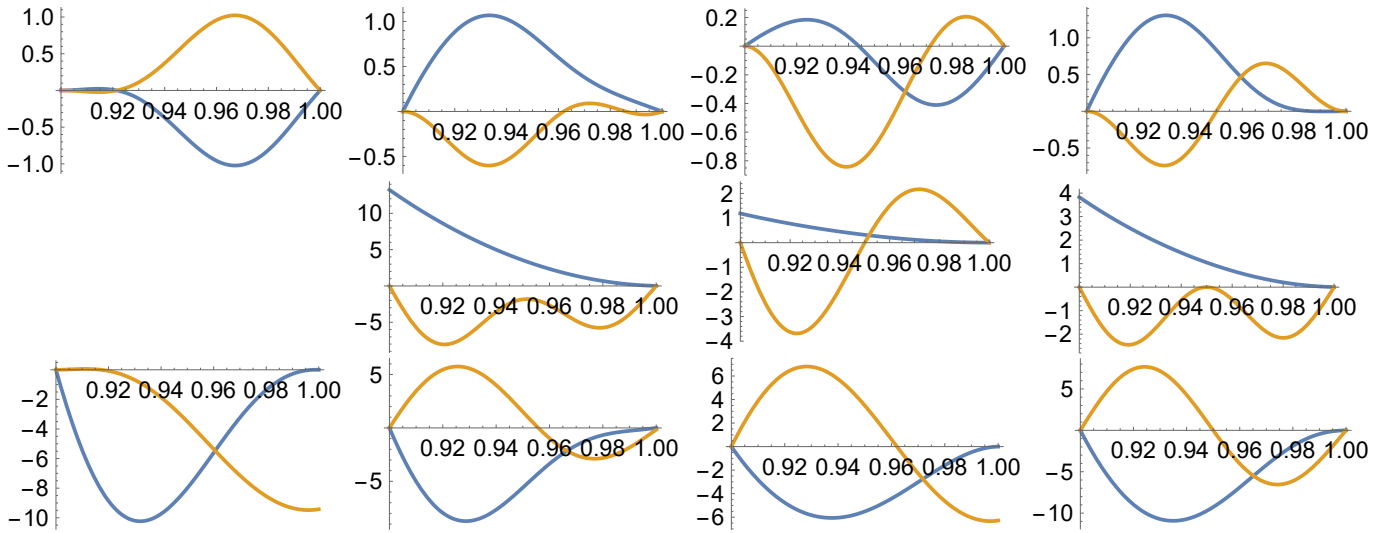


Figure 7. The $r\phi$, $\theta\phi$, and $r\theta$ components for Model IV are shown from the top to bottom rows. The spherical harmonics index from the left to right panels corresponds to $l = 1$ to 4.

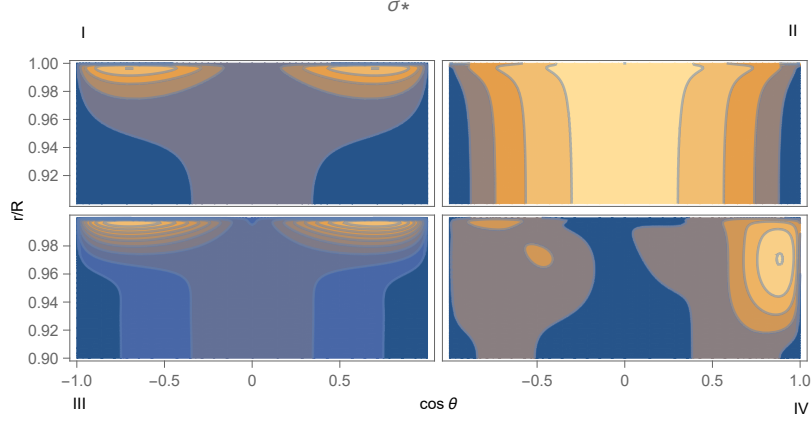


Figure 8. The magnitudes of the strain tensor normalized by the maximum are shown on the $\cos \theta - r/R$ plain for Models I–IV.

complex. The maximum of σ_* is located near the surface, or the position is shifted to the outer part compared with that of $|T_{\text{ela}}^{ij}|$ because the shear modulus μ decreases with the radius.

The stable range of the crust is limited as $(\sigma_{ij}\sigma^{ij}/2)^{1/2} < \sigma_c$, where σ_c is a number $\sigma_c \approx 10^{-2} - 10^{-1}$ (Horowitz & Kadau 2009; Baiko & Chugunov 2018; Caplan et al. 2018). This condition results in the upper limit of the field strength because $\sigma_{ij} \propto B_0^2/\mu_c$. The overall magnetic field strength B_0 is constrained as $B_0 < N_a (\sigma_c/0.1)^{1/2} \times 10^{14}\text{G}$, where N_a is a number that depends on the models, $N_{\text{I}} = 2.3$, $N_{\text{II}} = 5.1$, $N_{\text{III}} = 0.98$, and $N_{\text{IV}} = 1.1$. Similar constraints for the overall magnetic field strength are also obtained using different numerical methods for various magnetic fields (Kojima et al. 2022; Fujisawa et al. 2023). The precise value N_a and the failure position are determined by solving the differential equations for the magnetic field geometry, although the magnitude $N_a = \mathcal{O}(1)$ is simply estimated.

4. DISCUSSION

The elastic deformation of the crust due to magnetic stress is considered. The crustal strain was obtained by solving the differential equations with the appropriate boundary conditions. This study aims to compare the results with those obtained using the algebraic approximation in previous studies without any justification. The validity of the algebraic approximation was tested. The results of this study demonstrate that the algebraic expression never represents the correct elastic tensor. The resultant profile of the elastic stress is smoother than the magnetic one given as the source term. The radial variation is remarkable owing to the thin crust; however, it becomes less sharp when the differential equations are solved; the source term spreads globally in the solution. The magnitude of the elastic stress is generally smaller than that of the magnetic stress. The elastic stress is significantly smaller, especially in the diagonal components. Therefore, the elastic stress tensor cannot be approximated by any algebraic expression from the magnetic stress. Moreover, it is necessary to revisit evolution calculations which used the spurious criteria (Perna & Pons 2011; Viganò et al. 2013; Lander & Gourgouliatos 2019; Dehman et al. 2020; Gourgouliatos & Lander 2021). The present method for calculating the elastic tensor will be useful for improving the models. In numerical simulation of the magnetic field evolution, σ^{ij} is monitored by solving differential equations. Compared with an algebraic relation, this method significantly increases computing time, but is an inevitable step for examining the elastic limit of the crust.

The reason the algebraic expression disagrees with the correct result is discussed here. In the axially symmetric model, two components $\sigma^{r\phi}$ and $\sigma^{\theta\phi}$ relevant to the axial part are described by a single function ξ_ϕ , and satisfy $\sin \theta(\sigma^{r\phi}/\sin \theta)_{,\theta} = r(\sigma^{\theta\phi})_{,r}$ (see Equation (14)). The magnetic field is conveniently expressed by two functions Ψ and $S(\equiv r \sin \theta B_\phi)$, with the two components of the magnetic stress given by $(T_{\text{mag}}^{r\phi}, T_{\text{mag}}^{\theta\phi}) = S/(4\pi r^2 \sin^2 \theta)[\vec{\nabla}\Psi \times \vec{e}_\phi]$. The differential relation in which $(\sigma^{r\phi}, \sigma^{\theta\phi})$ are substituted by $-(2\mu)^{-1}(T_{\text{mag}}^{r\phi}, T_{\text{mag}}^{\theta\phi})$ does not hold, or strongly constrains Ψ and S ². Therefore, the algebraic relation $T_{\text{elas}}^{i\phi} + T_{\text{mag}}^{i\phi} = 0$ ($i = r, \theta$) is not compatible. The argument for the polar

² T_{mag}^{ij} is the difference between two states, and the constraint is for the initial states (Ψ, S) and their changes $(\delta\Psi, \delta S)$.

part is complex, but the relation $T_{\text{elas}}^{ij} + T_{\text{mag}}^{ij} = 0$ is satisfied only under restrictive conditions. One reason for this is that the material perturbation T_{hyd}^{ij} is induced. The pressure is significantly greater than the elastic and magnetic forces, so even a slight change in pressure perturbation significantly modifies the other forces. When restricting the class of displacement to neglect material perturbation, the four components σ^{rr} , $\sigma^{\theta\theta}$, $\sigma^{\phi\phi}$, and $\sigma^{r\theta}$ are expressed by two functions, ξ_r and ξ_θ , and are related to each other. The magnetic tensors T_{mag}^{rrr} , $T_{\text{mag}}^{\theta\theta}$, $T_{\text{mag}}^{\phi\phi}$, and $T_{\text{mag}}^{r\theta}$ are expressed by the 'square' of Ψ and S . Therefore, the linear relation $T_{\text{elas}}^{ij} + T_{\text{mag}}^{ij} = 0$ is not globally satisfied.

The elastic deviation due to magnetic stress is widespread, and is described by a solution of differential equations to be fitted to boundary conditions. The elastic response is not approximated by solely considering the local magnetic stress, however the explicit calculations given in this study are inevitable. This study provided the correct crustal failure process according to the evolution of the magnetic field.

ACKNOWLEDGMENTS

This work was supported by JSPS KAKENHI Grant Numbers JP19K03850, JP23K03389.

REFERENCES

- Aschwanden, M. J. 2015, *ApJ*, 814, 19, doi: [10.1088/0004-637X/814/1/19](https://doi.org/10.1088/0004-637X/814/1/19)
- Aschwanden, M. J., Crosby, N. B., Dimitropoulou, M., et al. 2016, *SSRv*, 198, 47, doi: [10.1007/s11214-014-0054-6](https://doi.org/10.1007/s11214-014-0054-6)
- Baiko, D. A., & Chugunov, A. I. 2018, *MNRAS*, 480, 5511, doi: [10.1093/mnras/sty2259](https://doi.org/10.1093/mnras/sty2259)
- Bak, P., Christensen, K., Danon, L., & Scanlon, T. 2002, *PhRvL*, 88, 178501, doi: [10.1103/PhysRevLett.88.178501](https://doi.org/10.1103/PhysRevLett.88.178501)
- Bak, P., Tang, C., & Wiesenfeld, K. 1987, *PhRvL*, 59, 381, doi: [10.1103/PhysRevLett.59.381](https://doi.org/10.1103/PhysRevLett.59.381)
- Beloborodov, A. M., & Levin, Y. 2014, *ApJL*, 794, L24, doi: [10.1088/2041-8205/794/2/L24](https://doi.org/10.1088/2041-8205/794/2/L24)
- Bochenek, C. D., Ravi, V., Belov, K. V., et al. 2020, *Nature*, 587, 59, doi: [10.1038/s41586-020-2872-x](https://doi.org/10.1038/s41586-020-2872-x)
- Caplan, M. E., Schneider, A. S., & Horowitz, C. J. 2018, *PhRvL*, 121, 132701, doi: [10.1103/PhysRevLett.121.132701](https://doi.org/10.1103/PhysRevLett.121.132701)
- Chamel, N., & Haensel, P. 2008, *Living Reviews in Relativity*, 11, 10, doi: [10.12942/lrr-2008-10](https://doi.org/10.12942/lrr-2008-10)
- Cheng, B., Epstein, R. I., Guyer, R. A., & Young, A. C. 1996, *Nature*, 382, 518, doi: [10.1038/382518a0](https://doi.org/10.1038/382518a0)
- CHIME/FRB Collaboration, Andersen, B. C., Bandura, K. M., et al. 2020, *Nature*, 587, 54, doi: [10.1038/s41586-020-2863-y](https://doi.org/10.1038/s41586-020-2863-y)
- Dehman, C., Viganò, D., Rea, N., et al. 2020, *ApJL*, 902, L32, doi: [10.3847/2041-8213/abbda9](https://doi.org/10.3847/2041-8213/abbda9)
- Du, Y.-Q., Wang, P., Song, L.-M., & Xiong, S.-L. 2024, *MNRAS*, 531, L57, doi: [10.1093/mnras/lsae031](https://doi.org/10.1093/mnras/lsae031)
- Dănilă, B., Harko, T., & Mocanu, G. 2015, *MNRAS*, 453, 2982, doi: [10.1093/mnras/stv1821](https://doi.org/10.1093/mnras/stv1821)
- Duncan, R. C., & Thompson, C. 1992, *ApJL*, 392, L9, doi: [10.1086/186413](https://doi.org/10.1086/186413)
- Esposito, P., Rea, N., & Israel, G. L. 2021, in *Astrophysics and Space Science Library*, Vol. 461, Astrophysics and Space Science Library, ed. T. M. Belloni, M. Méndez, & C. Zhang, 97–142, doi: [10.1007/978-3-662-62110-3_3](https://doi.org/10.1007/978-3-662-62110-3_3)
- Fujisawa, K., Kojima, Y., & Kisaka, S. 2023, *MNRAS*, 519, 3776, doi: [10.1093/mnras/stac3750](https://doi.org/10.1093/mnras/stac3750)
- Giliberti, E., Cambiotti, G., Antonelli, M., & Pizzochero, P. M. 2020, *MNRAS*, 491, 1064, doi: [10.1093/mnras/stz3099](https://doi.org/10.1093/mnras/stz3099)
- Gittins, F., Andersson, N., & Jones, D. I. 2021, *MNRAS*, 500, 5570, doi: [10.1093/mnras/staa3635](https://doi.org/10.1093/mnras/staa3635)
- Gourgouliatos, K. N., & Lander, S. K. 2021, *MNRAS*, 506, 3578, doi: [10.1093/mnras/stab1869](https://doi.org/10.1093/mnras/stab1869)
- Gögüş, E., Woods, P. M., Kouveliotou, C., et al. 1999, *ApJL*, 526, L93, doi: [10.1086/312380](https://doi.org/10.1086/312380)
- Gögüş, E., Woods, P. M., Kouveliotou, C., et al. 2000, *ApJL*, 532, L121, doi: [10.1086/312583](https://doi.org/10.1086/312583)
- Horowitz, C. J., & Kadau, K. 2009, *PhRvL*, 102, 191102, doi: [10.1103/PhysRevLett.102.191102](https://doi.org/10.1103/PhysRevLett.102.191102)
- Jones, P. B. 2003, *ApJ*, 595, 342, doi: [10.1086/377351](https://doi.org/10.1086/377351)
- Kaspi, V. M., & Beloborodov, A. M. 2017, *ARA&A*, 55, 261, doi: [10.1146/annurev-astro-081915-023329](https://doi.org/10.1146/annurev-astro-081915-023329)
- Kerin, A. D., & Melatos, A. 2022, *MNRAS*, 514, 1628, doi: [10.1093/mnras/stac1351](https://doi.org/10.1093/mnras/stac1351)
- Kojima, Y. 2022, *ApJ*, 938, 91, doi: [10.3847/1538-4357/ac9184](https://doi.org/10.3847/1538-4357/ac9184)
- Kojima, Y., Kisaka, S., & Fujisawa, K. 2021, *MNRAS*, 506, 3936, doi: [10.1093/mnras/stab1848](https://doi.org/10.1093/mnras/stab1848)
- . 2022, *MNRAS*, 511, 480, doi: [10.1093/mnras/stac036](https://doi.org/10.1093/mnras/stac036)
- . 2023, *ApJ*, 946, 75, doi: [10.3847/1538-4357/acc06b](https://doi.org/10.3847/1538-4357/acc06b)
- Landau, L. D., & Lifshitz, E. M. 1970, *Theory of elasticity* (2d ed.; Pergamon Press: Oxford)
- Lander, S. K. 2016, *ApJL*, 824, L21, doi: [10.3847/2041-8205/824/2/L21](https://doi.org/10.3847/2041-8205/824/2/L21)

- . 2023, *ApJL*, 947, L16, doi: [10.3847/2041-8213/acca1f](https://doi.org/10.3847/2041-8213/acca1f)
- Lander, S. K., Andersson, N., Antonopoulou, D., & Watts, A. L. 2015, *MNRAS*, 449, 2047, doi: [10.1093/mnras/stv432](https://doi.org/10.1093/mnras/stv432)
- Lander, S. K., & Gourgouliatos, K. N. 2019, *MNRAS*, 486, 4130, doi: [10.1093/mnras/stz1042](https://doi.org/10.1093/mnras/stz1042)
- Levin, Y., & Lyutikov, M. 2012, *MNRAS*, 427, 1574, doi: [10.1111/j.1365-2966.2012.22016.x](https://doi.org/10.1111/j.1365-2966.2012.22016.x)
- Lyutikov, M. 2003, *MNRAS*, 346, 540, doi: [10.1046/j.1365-2966.2003.07110.x](https://doi.org/10.1046/j.1365-2966.2003.07110.x)
- Makishima, K., Enoto, T., Hiraga, J. S., et al. 2014, *PhRvL*, 112, 171102, doi: [10.1103/PhysRevLett.112.171102](https://doi.org/10.1103/PhysRevLett.112.171102)
- Makishima, K., Enoto, T., Murakami, H., et al. 2016, *PASJ*, 68, S12, doi: [10.1093/pasj/psv097](https://doi.org/10.1093/pasj/psv097)
- Makishima, K., Enoto, T., Yoneda, H., & Odaka, H. 2021a, *MNRAS*, 502, 2266, doi: [10.1093/mnras/stab149](https://doi.org/10.1093/mnras/stab149)
- Makishima, K., Tamba, T., Aizawa, Y., et al. 2021b, *ApJ*, 923, 63, doi: [10.3847/1538-4357/ac28fd](https://doi.org/10.3847/1538-4357/ac28fd)
- McDermott, P. N., van Horn, H. M., & Hansen, C. J. 1988, *ApJ*, 325, 725, doi: [10.1086/166044](https://doi.org/10.1086/166044)
- Perna, R., & Pons, J. A. 2011, *ApJL*, 727, L51, doi: [10.1088/2041-8205/727/2/L51](https://doi.org/10.1088/2041-8205/727/2/L51)
- Petroff, E., Hessels, J. W. T., & Lorimer, D. R. 2022, *A&A Rv*, 30, 2, doi: [10.1007/s00159-022-00139-w](https://doi.org/10.1007/s00159-022-00139-w)
- Sang, Y., & Lin, H.-N. 2022, *MNRAS*, 510, 1801, doi: [10.1093/mnras/stab3600](https://doi.org/10.1093/mnras/stab3600)
- Suvorov, A. G., & Kokkotas, K. D. 2019, *MNRAS*, 488, 5887, doi: [10.1093/mnras/stz2052](https://doi.org/10.1093/mnras/stz2052)
- Thompson, C., & Duncan, R. C. 1995, *MNRAS*, 275, 255, doi: [10.1093/mnras/275.2.255](https://doi.org/10.1093/mnras/275.2.255)
- Thompson, C., Yang, H., & Ortiz, N. 2017, *ApJ*, 841, 54, doi: [10.3847/1538-4357/aa6c30](https://doi.org/10.3847/1538-4357/aa6c30)
- Totani, T., & Tsuzuki, Y. 2023, *MNRAS*, 526, 2795, doi: [10.1093/mnras/stad2532](https://doi.org/10.1093/mnras/stad2532)
- Tsuzuki, Y., Totani, T., Hu, C.-P., & Enoto, T. 2024, *MNRAS*, 530, 1885, doi: [10.1093/mnras/stae965](https://doi.org/10.1093/mnras/stae965)
- Turolla, R., Zane, S., & Watts, A. L. 2015, *Reports on Progress in Physics*, 78, 116901, doi: [10.1088/0034-4885/78/11/116901](https://doi.org/10.1088/0034-4885/78/11/116901)
- Ushomirsky, G., Cutler, C., & Bildsten, L. 2000, *MNRAS*, 319, 902, doi: [10.1046/j.1365-8711.2000.03938.x](https://doi.org/10.1046/j.1365-8711.2000.03938.x)
- Viganò, D., Rea, N., Pons, J. A., et al. 2013, *MNRAS*, 434, 123, doi: [10.1093/mnras/stt1008](https://doi.org/10.1093/mnras/stt1008)
- Wei, J.-J., Wu, X.-F., Dai, Z.-G., et al. 2021, *ApJ*, 920, 153, doi: [10.3847/1538-4357/ac2604](https://doi.org/10.3847/1538-4357/ac2604)
- Yamasaki, S., Göğüş, E., & Hashimoto, T. 2024, *MNRAS*, 528, L133, doi: [10.1093/mnras/lsad184](https://doi.org/10.1093/mnras/lsad184)
- Yang, Y.-P., & Zhang, B. 2021, *ApJ*, 919, 89, doi: [10.3847/1538-4357/ac14b5](https://doi.org/10.3847/1538-4357/ac14b5)
- Zhang, B. 2020, *Nature*, 587, 45, doi: [10.1038/s41586-020-2828-1](https://doi.org/10.1038/s41586-020-2828-1)
- Zhang, Y.-K., Li, D., Feng, Y., et al. 2024, *Science Bulletin*, 69, 1020, doi: [10.1016/j.scib.2024.02.010](https://doi.org/10.1016/j.scib.2024.02.010)